

Water Masers Toward Ultracompact HII Regions

S. Kurtz

*Centro de Radioastronomía y Astrofísica, UNAM, Apartado Postal 3-72, 58089, Morelia,
Michoacán, México*

s.kurtz@astrosmo.unam.mx

and

P. Hofner

*Physics Department, New Mexico Institute of Technology, Socorro, NM 87801; and
National Radio Astronomy Observatory, P.O. Box O, Socorro, NM 87801*

phofner@nrao.edu

ABSTRACT

We present a survey in the $6_{16} - 5_{23}$ rotational H_2O transition toward 33 galactic ultracompact HII regions. Maser emission is detected toward 18 of these sources; two are new detections. High quality spectra are provided for all 18 sources. We discuss the detection rate of this survey and the correlation of various maser properties with other physical parameters. In addition, we report wide-bandwidth (316 km s^{-1}), moderate-resolution ($\sim 3''$) H_2O maser observations of the HH80-81 region. We report the first detection of water maser emission at the approximate velocity of the molecular core. This emission is coincident with the extreme tip of the thermal jet, and well-removed from the much stronger and well-known maser emission at the position of VLA-3.

Subject headings: HII Regions — Masers — Stars: Formation — ISM: Herbig-Haro Objects

1. Introduction

Since their discovery over 30 years ago, water masers have been found in a variety of astronomical settings, primarily, but not exclusively, in the environs of evolved stars and of star-forming regions. Extensive surveys and classifications of water masers have been made

(for the northern hemisphere) by researchers at the Arcetri Observatory, including Cesaroni et al. (1988), Comoretto et al. (1990), Palagi et al. (1993), Brand et al. (1994), Valdetaro et al. (2001), and Brand et al. (2003). References to a number of southern surveys may be found in Braz et al. (1989). Additional studies, focusing on particular classes of objects, include Wouterloot & Walmsley (1986), Churchwell, Walmsley & Cesaroni (1990); Palla et al. (1991, 1993); Felli, Palagi, & Tofani (1992), Henning et al. (1992); Palumbo et al. (1994); Codella, Felli, & Natale (1996, and references therein), Hofner and Churchwell (1996), Furuya et al. (2003), and de Gregorio-Monsalvo et al. (2004). The present work extends the study of water masers in a well-defined sample of objects, in particular, water masers near ultracompact (UC) HII regions.

Studies too numerous to cite have found that water masers can trace circumstellar disks, molecular outflows, and ionized jets, all of which may be present at some moment during the massive star formation process. In some star-forming regions water masers are found in close proximity (often in projection against) the ionized gas of HII regions (e.g., Hofner & Churchwell 1996). However, in most cases, water masers seem to be physically associated with warm molecular gas, avoiding the HII region (e.g., Cesaroni et al. 1994). Trends in the coincidence of water, methanol, and hydroxyl masers have been interpreted to reflect an evolutionary sequence in the star formation process (see the discussions in Garay & Lizano 1999 and Beuther et al. 2002).

Despite the abundance of observational data and significant theoretical understanding of the pumping mechanisms (e.g., Kylafis & Norman 1991, and Elitzur, Hollenbach & McKee 1989), water masers continue to challenge our understanding, precisely because of the multiple phenomena that they trace. Further clarification of the physical role of water masers in the proximity of UC HII regions is needed, and the present work is intended to contribute to this topic.

In this paper we present the results of a single-dish survey of 33 UC HII regions and an interferometric study of one of these — HH80-81, also known as GGD 27 and G10.84–2.59. In §§2 and 3 we describe the single-dish observations and discuss their results. In §4 we present the interferometric observations and discuss their results. We summarize our findings in §5.

2. SINGLE-DISH OBSERVATIONS AND DATA REDUCTION

Observations of the $6_{16} - 5_{23}$ rotational transition of H_2O were obtained on 1995 September 22 – 24 with the 100 m telescope of the Max Planck Institute for Radioastronomy near

Effelsberg, Germany. We used the facility 1.3 cm receiver and the 1024 channel autocorrelator. System temperatures ranged from 140 to 280 K. We observed with bandwidths of 25 and 12.5 MHz, which provide resolutions of 0.33 and 0.17 km s⁻¹ respectively. The half-power beamwidth, measured through cross-scans on strong point sources, was about 40". Flux calibration was based on observations of NGC 7027, for which we assumed a flux density of 5.86 Jy. An elevation dependent gain correction was applied to the data. We observed the strong source G34.26+0.15 daily to monitor the influence of varying weather conditions on the calibration. From these observations we conclude that the calibration accuracy is better than 25%. Pointing corrections were obtained every hour from cross-scans of strong point sources at small angular distances from the program sources; typical corrections were 5".

Our candidate sources were taken from Kurtz, Churchwell & Wood 1994 (hereafter KCW). Table 1 lists the observed sources in column 1. Columns 2 and 3 give the pointing position in equatorial coordinates, column 4 indicates the range of observed LSR velocities, and column 5 reports our detection limits. The median 3 σ detection limit was 0.34 Jy. In column 6 we indicate whether water masers were detected.

The spectra were baseline subtracted, summed, and smoothed to a final resolution of 0.33 km s⁻¹. In Table 2 we report the observed parameters of the detected masers. In column 1 we list the source name, while columns 2 and 3 give the flux density and LSR velocity of the strongest feature in the spectrum. In column 4 we list the velocity range over which emission in the H₂O line was detected and in column 5 the velocity-integrated flux density of the strongest feature.

3. SINGLE-DISH RESULTS

Maser emission was detected in 18 of the 33 sources observed; a 55% detection rate. Two of these, G11.11–0.40 and G18.30–0.39 are new detections, not previously reported in the literature. The spectra of all 18 sources are shown in Figure 1.

3.1. Variability

Variability of water masers is well-known and our observations confirm this in a number of cases. Four sources show particularly strong variations. G10.84–2.59 shows a flux density of 205 Jy in our observations. It is reported at 8 Jy by Martí, Rodríguez & Torrelles (1999), and 53 Jy by Cesaroni et al. (1988), while Codella et al. (1995) report a null detection with an upper limit of 3.6 Jy. We detect a 4 Jy maser in the G35.02+0.35 field, for which Cesaroni

et al. (1988) report 63 Jy. G80.87+0.42 is undetected by us and by Palla et al. (1991) but a 106 Jy detection is reported by Han et al. (1998). G106.8+5.31 we detect with 15 Jy, while Comoretto et al. (1990) detected 27 Jy and Cesaroni et al. (1988) report 250 Jy.

The impact of variability on our detection rate is not clear. Of the 15 null detections we report, 13 (all but G9.88–0.75 and G18.15–0.28) have observations reported in the literature. Of the 13, only two (G80.87+0.42 and G111.28–0.66) have reported detections. Using a simple statistical argument, applicable to their sample, Miralles, Rodríguez & Scalise (1994) argue that essentially all sources in their sample may show water maser emission at some point, with null detections arising from variability. The Miralles et al. sample was quite similar to our own in the sense that both are constituted of high mass star formation regions; hence it is possible that most of the 15 null detections we report do harbor water masers.

3.2. Maser Velocities

In figure 2 we plot the maser line velocities versus associated molecular line velocities. Except for G10.84–2.59 and G106.80+5.31, the molecular gas velocities are taken from the CS observations of Bronfman, Nyman & May (1996). For the two sources mentioned, CS data are not available; CO velocities are used instead (Kurtz 1993). As expected, the molecular line velocities and the maser velocities are in generally good agreement, with a median difference of 4.5 km s^{-1} . The notable exception is G10.84–2.59, also known as GGD 27 and HH 80-81, which shows a $|V_{CO} - V_{H_2O}|$ of $\sim 85 \text{ km s}^{-1}$ for the peak maser component. The large blueshift of the peak maser component with respect to the ambient cloud was reported by Gómez, Rodríguez & Martí, (1995), who suggest that outflow activity may be occurring. Our spectrum shows maser emission ranging from -80.6 to $+4.2 \text{ km s}^{-1}$. Though relatively weak, the most redshifted maser component we detect differs from the cloud velocity by only 6.8 km s^{-1} (see §4.1). Prior high resolution (interferometric) observations of this region used relatively narrow bandpasses, centered near the strongest component at approximately -70 km s^{-1} , and thus did not detect the more redshifted components. To locate these components with respect to the blueshifted masers and the free-free emission sources in the field, we made moderate-resolution interferometric observations that we report in §4.

The velocity range of maser emission is also shown in figure 2. Two sources in our sample, G10.84–2.59 and G69.54–0.89, presented particularly broad ranges in maser velocities. For G10.84 the total range is 85 km s^{-1} (or 100 km s^{-1} including the VLA detection of §4) while for G69.54–0.89 the range was 116 km s^{-1} . We are unaware of broadband interferometric observations of G69.54–0.89 (ON-1), which would include the full 116 km s^{-1} range. Such

observations would be worthwhile, particularly to locate the extreme velocity components with respect to other star formation signposts in the field (e.g., Kumar, Tafalla & Bachiller 2004).

3.3. Correlations

No correlation was found between the free-free radio continuum flux densities and the peak maser component flux densities. No systematic trends with respect to the far-infrared (FIR) luminosity (taken from KCW) were seen, either in the detection/non-detection of masers, in the flux density of the strongest maser component, or in the velocity range over which maser emission was detected. Likewise the range of observed maser velocities showed no correlation with the free-free flux density, the strength of the peak maser component, the CS (or CO) linewidth, or *IRAS* colors.

We do find a trend for increasing maser luminosity with increasing far infrared luminosity. A linear fit provides results that are consistent, within the uncertainty, with the results of Wouterloot & Walmsley (1986), Palagi et al. (1993), and Miralles et al. (1994). Palagi et al. have a much larger sample and we consider their fit to be more reliable than our own.

Neither the null detections nor the detected sources showed evidence for correlation with *IRAS* colors. We note, however, that within our sample there were a number of sources with large F_{60}/F_{25} , F_{60}/F_{12} , and F_{25}/F_{12} ratios (with respect to the sample median); without exception these reddened sources showed maser emission. Large F_{100}/F_{60} ratios, however, are evenly mixed between detections and non-detections. These trends are in general agreement with the results of Palla et al. (1991) who found higher detection rates for redder sources.

3.4. Analysis of the Detection Rate

Numerous water maser surveys of star-forming regions have been made, several of which used selection criteria similar to our own. Three such studies are particularly relevant here: Churchwell, Walmsley & Cesaroni (1990, hereafter CWC), Palla et al. (1991, 1993), and Palumbo et al. (1994) and Codella et al. (1995).

The CWC source list was comprised of two parts: regions known to contain UC HII regions (64) and regions likely to contain UC HII regions (based on their *IRAS* colors), but not confirmed to contain them (20). They report a 67% water maser detection rate for the former group and a 65% detection rate for the latter group. Palla et al. (1991) found a 26% detection rate for their “high” group, which had *IRAS* 60 μm fluxes greater than

100 Jy and whose *IRAS* colors matched the selection criteria of Wood & Churchwell (1989, hereafter WC). These color criteria require that $\log (F_{60}/F_{12}) \geq 1.30$ and $\log (F_{25}/F_{12}) \geq 0.57$. Palumbo et al. (1994) and Codella et al. (1995) reviewed the literature and performed additional observations of regions with *IRAS* colors indicative of star-forming molecular cloud cores. Codella et al. identify 672 *IRAS* sources meeting the WC color criteria and report a water maser detection rate of 20%.

In the present work, we have used the same WC color criteria as the other three surveys, and report a 55% detection rate. Thus, of four samples meeting the WC color criteria, the reported water maser detection rates are 67% (CWC), 55% (this paper), 26% (Palla et al. 1991) and 20% (Codella et al. 1995).

As noted by Palla et al. (1991), sensitivity may explain part of the differing detection rates. Our typical 3σ detection level, as that of CWC, is about a factor of 10 lower than the corresponding detection level of Palla et al. (1991) and Codella et al. (1995). Applying a 5 Jy cut-off level (typical of the detection levels of the other surveys) lowers our detection rate to 36% and that of CWC to 35%.

In addition, the CWC sample, and our own, are biased toward brighter infrared sources. Most of the CWC sources and all of our own have *IRAS* 100 μm flux densities greater than 1000 Jy. All of these sources have $F_{60 \mu m} > 100$ Jy, which is the flux cut-off proposed by Codella, Felli & Natale (1994) below which *IRAS* sources cannot be reliably associated with UC HII regions. This same flux limit, when imposed by Palla et al. (1993), more than halved their maser detection rate. Blind radio surveys, observing *IRAS* sources with WC colors in search of UC HII regions, suggest that the detection rate can fall from around 80% for bright sources, with $F_{100} > 1000$ Jy, to around 40% for dimmer sources, with $1000 \text{ Jy} > F_{100} > 100$ Jy (Kurtz 1995). It is plausible that the difference of 10-15% in the detection rates, after allowing for sensitivity effects, might result from a lower success rate of the color selection criteria for weaker sources.

A reasonable interpretation is that the CWC detection rate, and the rate we report here, are representative of the fractional lifetime during which massive star formation regions with UC HII regions exhibit detectable (i.e., allowing for variability) maser emission. On the other hand, the relatively low rates reported by Palla et al. (1991, 1993) and by Codella et al. (1995) probably reflect their lower sensitivity and imperfections in the WC color selection criteria for weak *IRAS* sources. I.e., differing selection criteria and differing sensitivities are the probable explanation for the distinctly different detection rates.

Our sample is small and deliberately biased toward star-forming regions that have already formed massive stars. It is likely that water masers occur in younger (proto-stellar)

objects, but our results cannot be taken to represent isolated earlier evolutionary stages. Rather, they represent the typical case of massive star-forming regions where several different evolutionary stages are present at the same time.

4. VLA OBSERVATIONS of HH80-81

4.1. Motivation and Observational Details

Following the original water maser detection in the HH80-81 region (G10.84–2.59; GGD 27) by Rodríguez et al. (1978), most observers have concentrated on the so-called “high velocity maser”, at $V_{lsr} \approx -70 \text{ km s}^{-1}$. Our high sensitivity 100 m spectrum shows evidence for maser emission at $V_{lsr} \approx +3 \text{ km s}^{-1}$, similar to the molecular core velocity of $+11 - +13 \text{ km s}^{-1}$ (Rodríguez et al. 1980, Gómez et al. 2003). The location of this “positive velocity maser” is interesting, particularly because the high velocity maser is *not* coincident with the thermal jet or its suspected driving source (Gómez, Rodríguez & Martí 1995). To locate the positive velocity maser, we made observations with the Very Large Array (VLA) of the NRAO¹ on 1999 June 3 and 1999 November 30. The June observations were at relatively low spatial and spectral resolution but with broad velocity coverage. The November observations offered less velocity coverage, but at higher spatial and spectral resolution. We describe the two observational periods below.

Observations were made on 1999 June 3 while the array was being reconfigured from the D to the A configuration. The two outermost antennas on each arm were not available for observations. Twenty antennas, at D-array stations, were used, resulting in a resolution of $4''.5 \times 2''.3$. Channel widths of 48.8 kHz provided a velocity resolution of 0.66 km s^{-1} . The data were edited and calibrated using standard AIPS procedures. Bandpass calibration was not applied to the data, nor was self-calibration performed. The flux density scale was set by observations of 3C286 with an adopted flux density of 2.518 Jy. The phase calibrator was 1820–254, with a bootstrapped flux density of 0.72 Jy. We observed in five overlapping bands of 127 channels, centered at LSR velocities of -158 , -92.5 , -30 , $+32.5$, and $+95 \text{ km s}^{-1}$. The velocities were chosen so that adjacent bands had 16 channels of overlap which were discarded without loss of velocity coverage. Each velocity dataset was imaged and cleaned with the AIPS task IMAGR, using uniform uv weighting with a robustness of -0.2 . The cubes were initially cleaned to a flux level of 5 times the theoretical *rms* and inspected

¹The National Radio Astronomy Observatory is a facility of the National Science Foundation operated under cooperative agreement by Associated Universities, Inc.

for maser emission. Channels with maser emission were then cleaned to a 2σ level. The resulting image cubes were merged to produce a single 480 channel cube with a velocity coverage of 316 km s^{-1} , from -190 to $+126 \text{ km s}^{-1}$.

The 1999 June observations detected a positive velocity maser but had inadequate spectral resolution to resolve the line. The maser was detected not at the $+3 \text{ km s}^{-1}$ of the 100-m detection, but rather at a velocity of $+20 \text{ km s}^{-1}$. To confirm the detection and to provide better line parameters, we re-observed this spectral feature with the VLA on 1999 November 30. The array was in the B-configuration ($0'.52 \times 0'.26$ resolution), and we observed for 14 min on-source, with a spectral resolution of 12.2 KHz (0.16 km s^{-1}) and 20 km s^{-1} bandwidth. No flux calibrator was observed, but inspection of the uv -data of the phase calibrator (1820–254) suggests its flux density was 1.1 Jy, which is consistent with values from VLA calibrator database during that period. We adopt this value, but caution that the absolute flux density calibration may have an uncertainty as large as 20%. No bandpass calibration was performed. Imaging followed the same procedures as the 1999 June observations.

4.2. Results: Maser Positions and Velocities

Two sites of maser emission were detected by our broad-band observations: the previously known, high-velocity maser coincident with VLA-3 (Gómez et al. 1995; Martí et al. 1999) and the newly detected $+20 \text{ km s}^{-1}$ maser. The maser at VLA-3 is substantially the stronger of the two and contains multiple velocity features (see figure 3). The $+20 \text{ km s}^{-1}$ maser is much weaker and shows a single velocity feature (see figure 4). The VLA-3 maser is about $5''$ to the east of the HH80-81 thermal jet axis, while the 20 km s^{-1} maser is aligned with the thermal jet (see figure 5).

The $+20 \text{ km s}^{-1}$ maser line profile was fully resolved by the 1999 November observations (see inset to figure 4). The gaussian line FWHM is 0.8 km s^{-1} with a central velocity of 19.9 km s^{-1} and a peak of 0.57 Jy. A two-dimensional gaussian fit to the peak channel yields a position of (B1950) R.A. $18^{\text{h}} 16^{\text{m}} 13.077^{\text{s}}$, Dec $-20^{\circ} 48' 45.46''$ or (J2000) R.A. $18^{\text{h}} 19^{\text{m}} 12.170^{\text{s}}$, Dec $-20^{\circ} 47' 28.09''$.

There have been significant changes in the velocity structure of the masers during the period 1995-99. First, we note that the 1 Jy feature at $+3 \text{ km s}^{-1}$ from the 100-m observations in 1995 was *not* detected by our VLA observations in 1999. Because of the low angular resolution of the 100-m data, no position information is available for the $+3 \text{ km s}^{-1}$ maser. It seems plausible that it was near the position of the newly detected 20 km s^{-1} maser, rather

than coincident with VLA 3, but this is not confirmed. The VLA-3 maser emission shows a significantly different velocity structure between the 1998 May observations of Martí et al. (1999) and our 1999 June observations. The Martí et al. spectrum (with a bandwidth from -90 to -48 km s^{-1}) shows emission from -72.6 to -50.2 km s^{-1} , with the strongest component at -61.1 km s^{-1} . Our spectrum shows the strongest component now at -86.0 km s^{-1} . Moreover, because of our wider bandwidth, we also detect maser emission at this position between -50 and -37 km s^{-1} (see figure 3).

4.3. Implications of the Newly Detected Maser Emission

Water masers have been observed numerous times in HH80-81, including Rodríguez et al. (1978), Rodríguez et al. (1980), Gómez et al. (1995), and Martí et al. (1999). Most of these observations concentrated on the high velocity component at VLA-3, and used a relatively narrow bandpass centered near -70 km s^{-1} . The velocity components that we detect in the range of -50 to -40 km s^{-1} are clearly associated with the VLA-3 continuum component. However, our broadband data lack the spatial resolution to resolve the distinct spectral components. Martí et al. 1999 resolved the VLA-3 maser emission into two clusters of components, one of which shows a linear structure. The intermediate velocity components that we detect might lend further insight into the nature of these two clumps; high angular resolution observations of these velocity components would be worthwhile. Although water masers are well-known to be variable, the differences between the published spectra of the VLA-3 masers are substantial. This strong variability is almost certainly relevant to the physical interpretation of these masers.

The positive velocity maser, at $+20$ km s^{-1} , may prove useful for our understanding of the thermal jet associated with HH80-81. The maser is clearly aligned with the axis of the thermal jet (figure 5). The location of the maser at the extremum of the jet continuum emission may indicate that the maser occurs at an interface region where the jet interacts with its surroundings. This interpretation is supported by the fact that the maser occurs at the edge of a molecular clump, seen in ammonia emission (Gómez et al. 2003). We note, however, that the maser is offset from IRS 2 by $\sim 1''.5$. (Stecklum et al. 1997). Radiative pumping mechanisms in dusty media have been proposed for water masers (e.g., Babkovskaia & Poutanen 2004). Thus, the maser may owe its existence to a nearby radiation source rather than to the interaction of the thermal jet with the ambient cloud material.

5. Summary

We present single-dish water maser observations toward 33 galactic ultracompact HII regions. We detect maser emission in 18 of these, two of which (G11.11–0.40 and G18.30–0.39) are new detections. Significant maser variability is noted for some sources. No correlations were found between various infrared and radio indicators and the presence, absence, strength, or velocity spread of maser emission. We do find a weak trend for increasing maser luminosity with increasing far infrared luminosity, in accord with trends previously reported in the literature. We compare the detection rate of this survey (55%) with those of other surveys, and find that the differences can be explained in terms of differing sensitivities and source selection criteria.

We also present interferometric water maser observations toward one source in our sample (G10.84–2.59, HH80-81, GGD 27) which presented an unusually broad range of velocity components. We report previously undetected, intermediate velocity maser emission, coincident with the source VLA-3. We also report the first detection of positive velocity maser emission at the tip of the thermal jet.

We thank F. Wyrowski for helpful discussions and L. F. Rodríguez and Y. Gómez for providing the 3.6 cm continuum and the ammonia maps of HH80-81. We particularly thank B. Clark for scheduling *ad hoc* VLA observations of the HH80-81 region. S.K. acknowledges financial support from DGAPA, UNAM project 118401 and Project 36568-E, CONACyT, México. P.H. acknowledges financial support from NSF grant AST-0454665 and Research Corporation grant CC4996. This research has made use of the SIMBAD database, operated at CDS, Strasbourg, France.

REFERENCES

- Babkovskaia, N., & Poutanen, J. 2004, *A&A*, 418, 117
- Beuther, H., Walsh, A., Schilke, P., Sridharan, T. K., Menten, K. M., & Wyrowski, F. 2002, *A&A*, 390, 289
- Brand, J., Cesaroni, R., Comoretto, G., Felli, M., Palagi, F., Palla, F., & Valdetaro, R. 2003, *A&A*, 407, 573
- Brand, J., et al. 1994, *A&AS*, 103, 541

- Braz, M. A., Scalise, E., Gregorio Hetem, J. C., Monteiro do Vale, J. L., & Gaylard, M. 1989, *A&AS*, 77, 465
- Bronfman, L., Nyman, L.-Å., & May, J. 1996, *A&AS*, 115, 81
- Cesaroni, R., Churchwell, E., Hofner, P., Walmsley, C. M., & Kurtz, S. 1994, *A&A*, 288, 903
- Cesaroni, R., Palagi, F., Felli, M., Catarzi, M., Comoretto, G., De Franco, S., Giovanardi, C., & Palla, F. 1988, *A&AS*, 76, 445
- Churchwell, E., Walmsley, C. M., & Cesaroni, R. 1990, *A&AS*, 83, 119 (CWC)
- Codella, C., Felli, M., & Natale, V. 1994, *A&A*, 284, 233.
- Codella, C., Felli, M., & Natale, V. 1996, *A&A*, 311, 971
- Codella, C., Palumbo, G.G.C., Pareschi, G., Scappini, F., Caselli, P., & Attolini, M.R. 1995, *MNRAS*, 276, 57
- Comoretto, G., et al. 1990, *A&AS*, 84, 179
- de Gregorio-Monsalvo, I., Gómez, Y. Anglada, G., Cesaroni, R., Miranda, L. F., Gómez, J. F., & Torrelles, J. M. 2004, *ApJ*, 601, 921
- Elitzur, M., Hollenbach, D. J., & McKee, C. F. 1989, *ApJ*, 346, 983
- Felli, M., Palagi, F., & Tofani, G. 1992, *A&A*, 255, 293
- Furuya, R. S., Kitamura, Y., Wootten, H. A., Claussen, M. J., & Kawabe, R. 2003, *ApJS*, 144, 71
- Garay, G., & Lizano, S. 1999, *PASP*, 111, 1049
- Gómez, Y., Rodríguez, L. F., Girart, J. M., Garay, G., & Martí, J. 2003, *ApJ*, 597, 414
- Gómez, Y., Rodríguez, L. F., & Martí, J. 1995, *ApJ*, 453, 268
- Han, F., Mao, R. Q., Lu, J., Wu, Y. F., Sun, J., Wang, J. S., Pei, C. C., Fan, Y., Tang, G. S., & Ji, H. R. 1998, *A&AS*, 127, 181
- Henning, T., Cesaroni, R., Walmsley, M., & Pfau, W. 1992, *A&AS*, 93, 525
- Hofner, P., & Churchwell, E. 1996, *A&AS*, 120, 283
- Kumar, M. S. N., Tafalla M., & Bachiller R. 2004, *A&A*, 426, 195

- Kurtz, S. 1995, *RMxAC*, 3, 39
- Kurtz, S. E., 1993, Ph.D. dissertation, Wisconsin
- Kurtz, S. E., Churchwell, E., & Wood, D.O.S. 1994, *ApJS*, 91, 659 (KCW)
- Kurtz, S., Hofner, P., & Vargas Álvarez, C. 2004, *ApJS*, 155, 149
- Kylafis, N. D., & Norman, C. A. 1991, *ApJ*, 373, 525
- Martí, J., Rodríguez, L. F., & Torrelles, J. M. 1999, *A&A*, 345, L5
- Miralles, M. P., Rodríguez, L. F., & Scalise, E. 1994, *ApJS*, 92, 173
- Palagi, F., Cesaroni, R., Comoretto, G., Felli, M., & Natale, V. 1993, *A&AS*, 101, 153
- Palla, F., Brand, J., Cesaroni, R., Comoretto, G., & Felli, M. 1991, *A&A*, 246, 249
- Palla, F., Cesaroni, R., Brand, J., Caselli, P., Comoretto, G., & Felli, M. 1993, *A&A*, 280, 599
- Palumbo, G.G.C., Scappini, F., Pareschi, G., Codella, C., Caselli, P., & Attolini, M.R. 1994, *MNRAS*, 266, 123
- Rodríguez, L. F., Moran, J. M., Dickinson, D. F., & Gyulbudaghian, A. L. 1978, *ApJ*, 226, 115
- Rodríguez, L. F., Moran, J. M., Ho, P. T. P., & Gottlieb, E. W. 1980, *ApJ*, 235, 845
- Stecklum, B., Feldt, M., Richichi, A., Calamai, G., & Lagage, P. O. 1997, *ApJ*, 479, 339
- Valdettaro, R., et al. 2001, *A&A*, 368, 845
- Wood, D.O.S., & Churchwell, E. 1989, *ApJ*, 340, 265 (WC)
- Wouterloot, J. G. A., & Walmsley, C. M. 1986, *A&A*, 168, 237

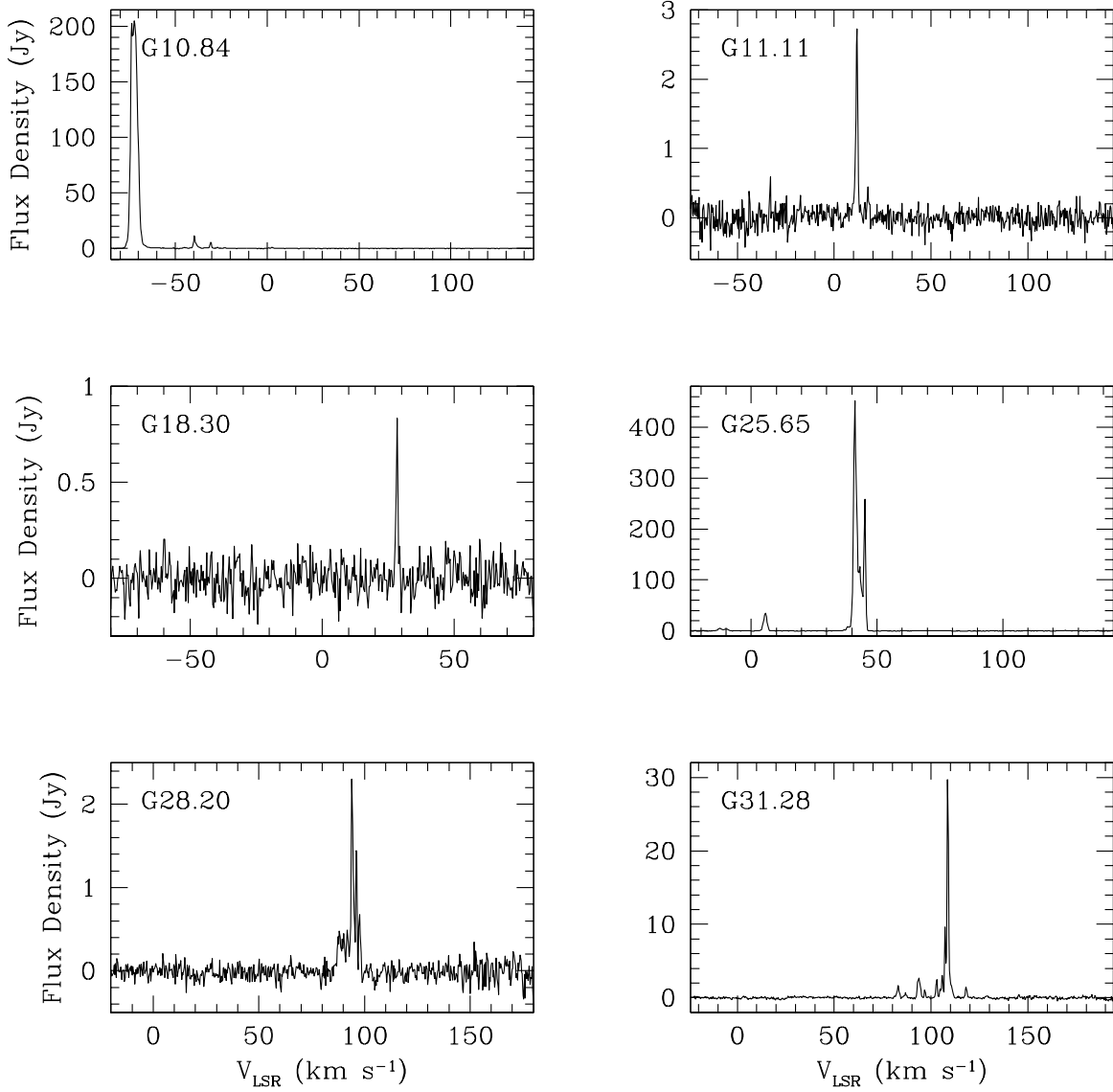


Fig. 1.— Single-dish spectra. Spectra were obtained with the 100 m telescope in 1995 September. The spectral resolution in all plots is 0.33 km s^{-1} . The median 1σ rms noise level is 0.11 Jy.

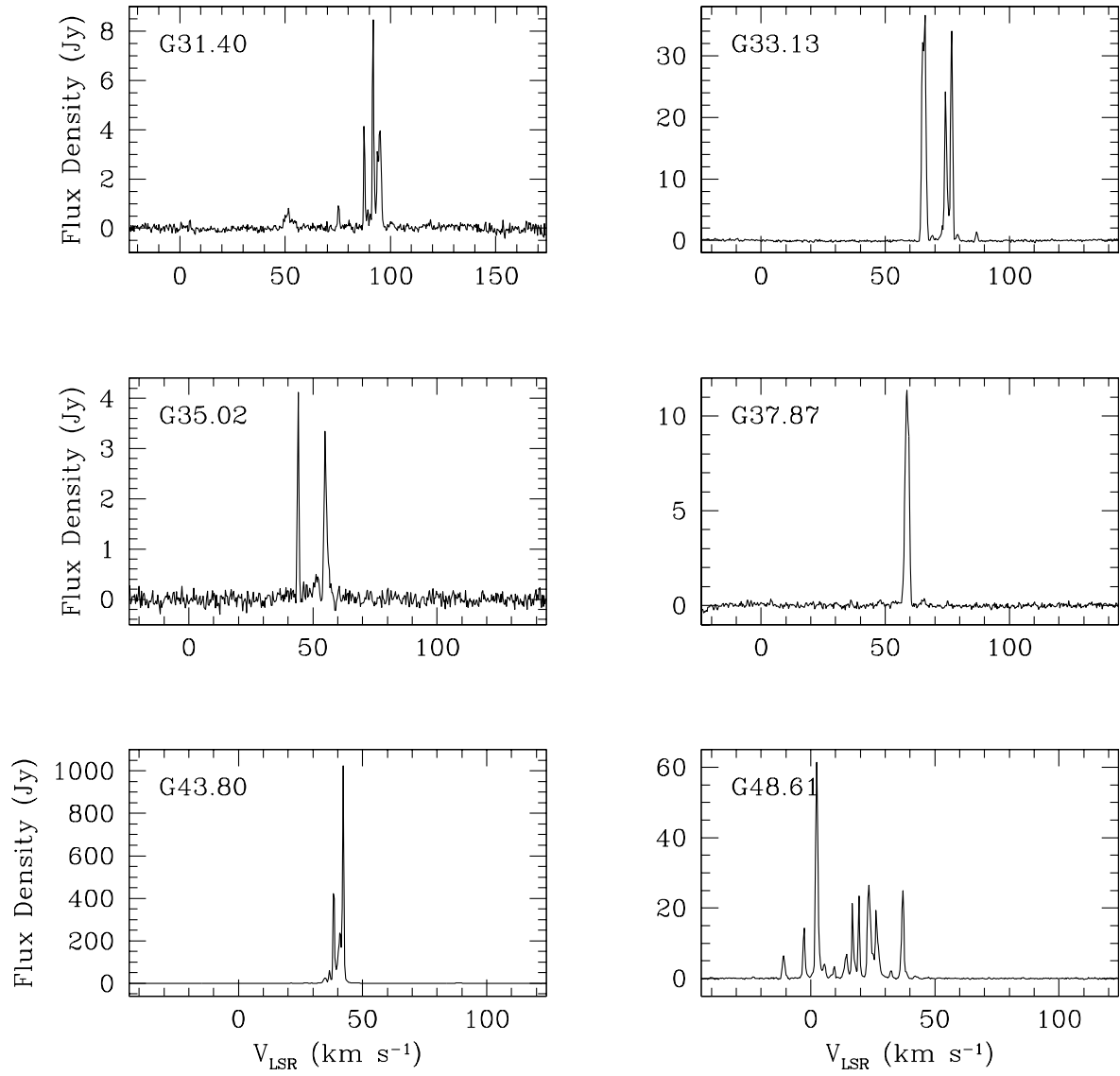


Fig. 1 continued.—

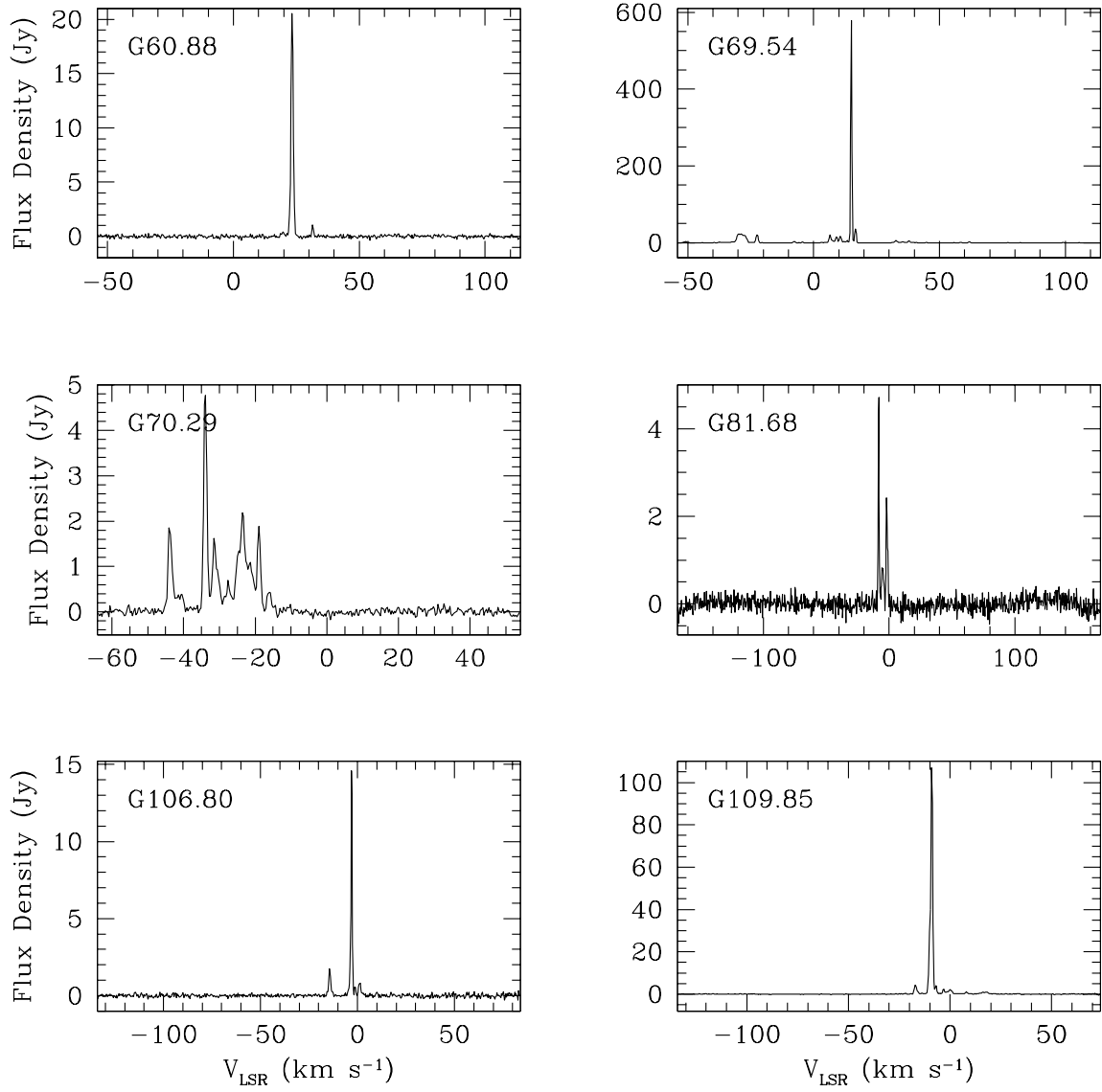


Fig. 1 continued.—

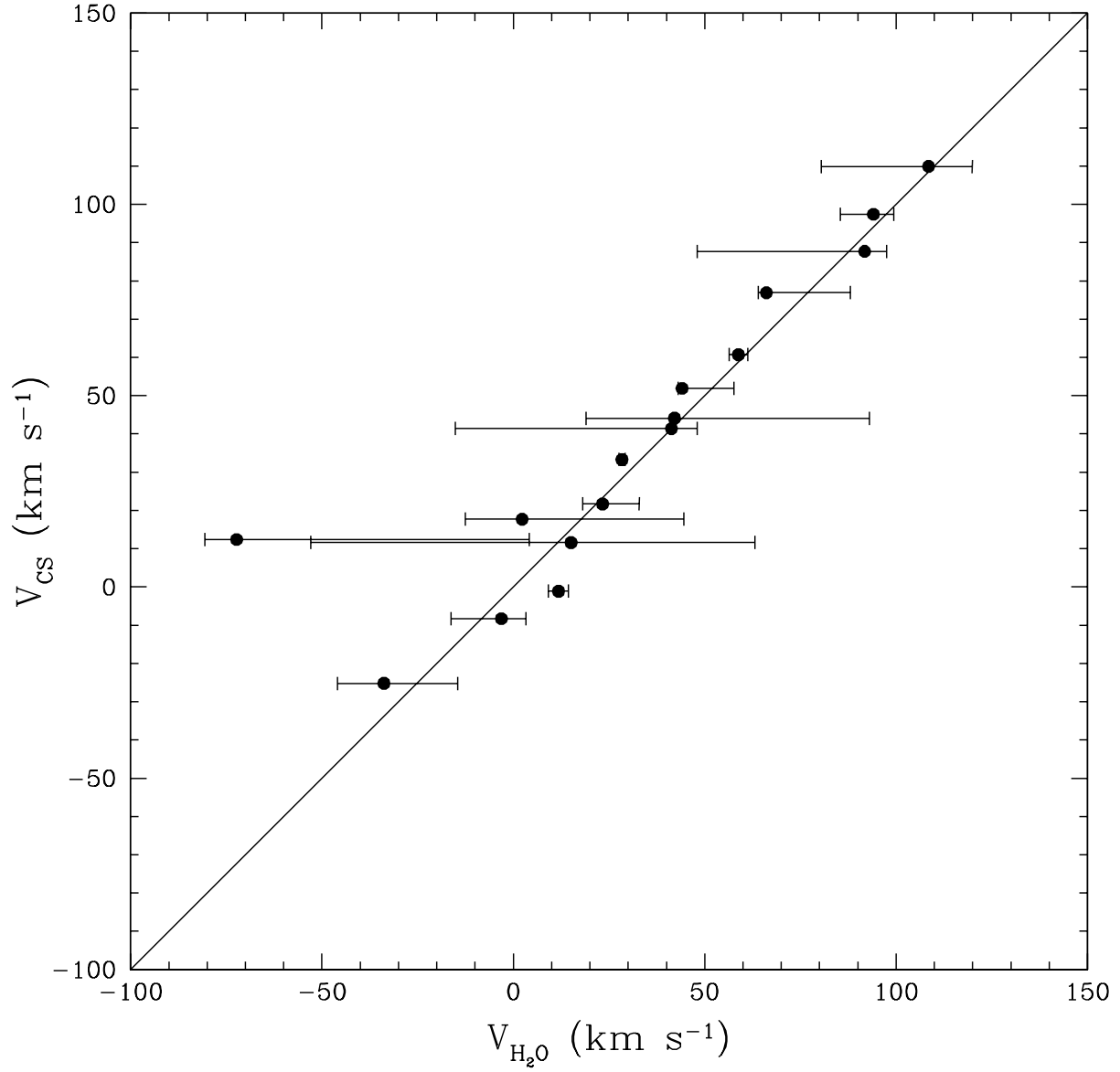


Fig. 2.— Water maser velocities compared to host molecular cloud CS velocities from Bronfman et al. (1996). The points show the peak maser component velocity (and the CS velocity) while the horizontal bars show the full range of maser velocity components.

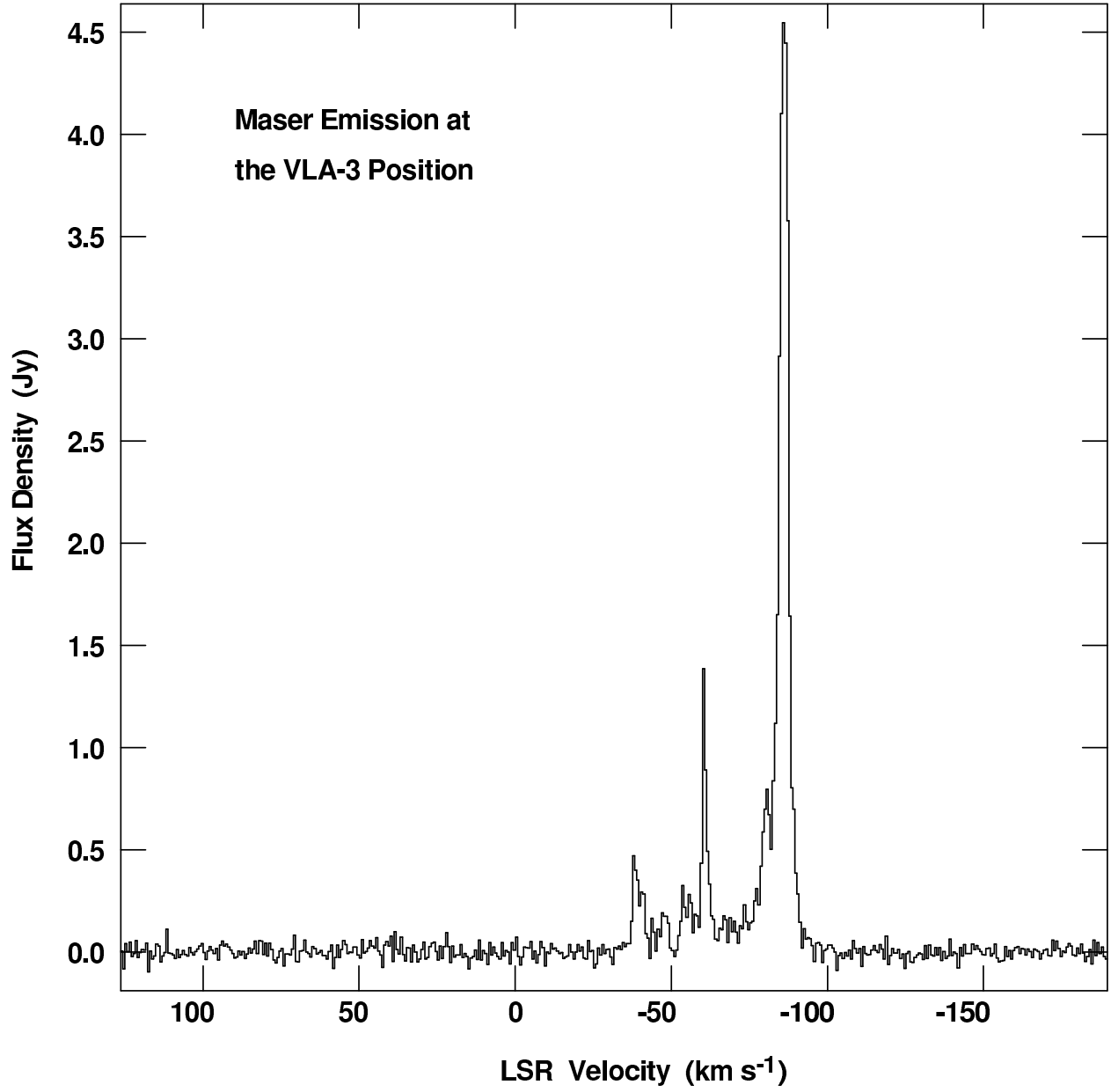


Fig. 3.— Broad-band maser spectrum at the position of VLA-3.

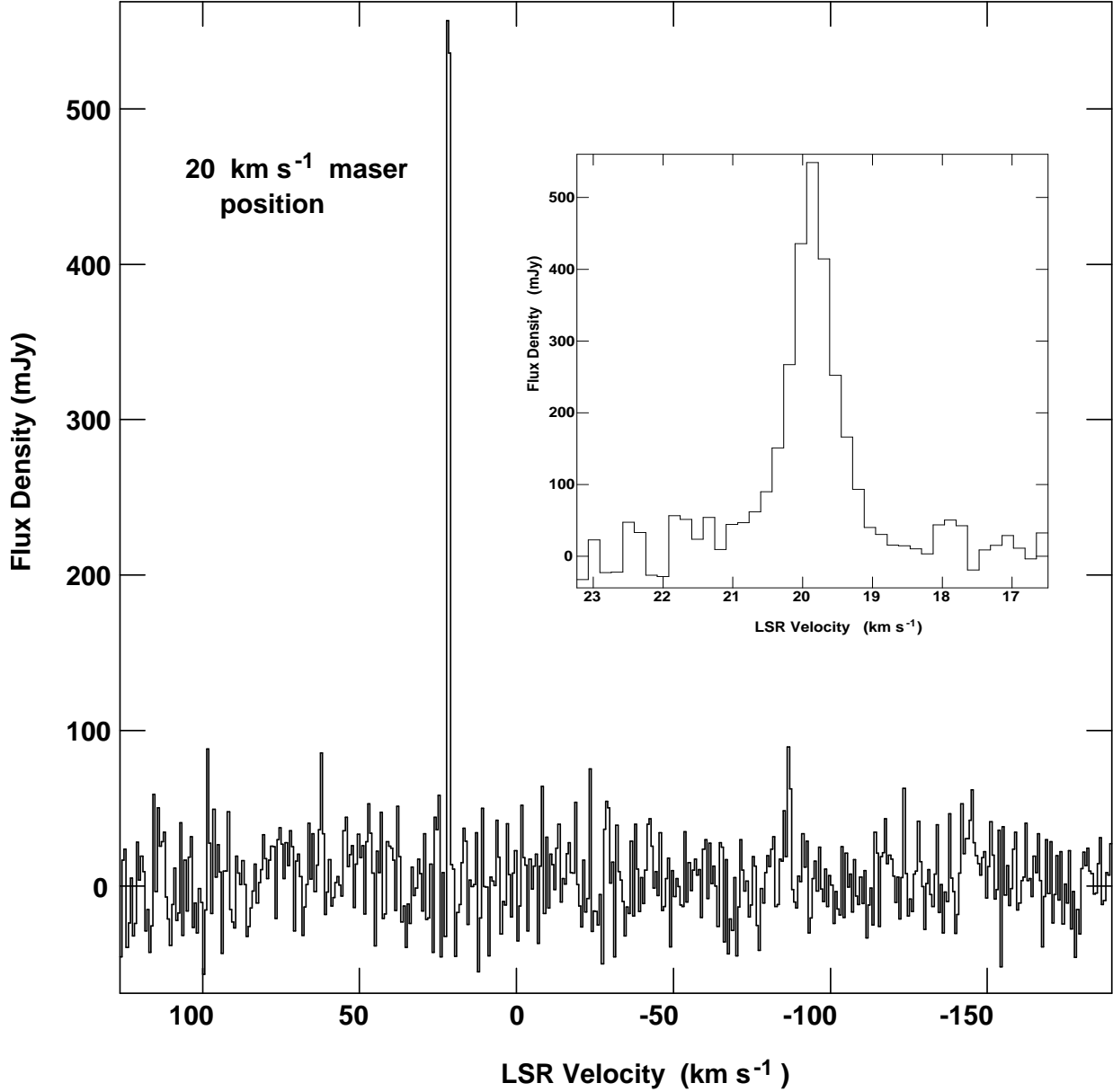


Fig. 4.— Broad-band and narrow-band (inset) spectra of the 20 km s^{-1} maser aligned with the thermal jet of G10.84–2.59 (HH80-81). The broad-band spectrum was obtained in 1999 June with angular resolution of $4''.5 \times 2''.3$ and spectral resolution of 0.66 km s^{-1} . The narrow-band spectrum (inset) was obtained in 1999 November with $0''.52 \times 0''.26$ angular resolution and 0.16 km s^{-1} spectral resolution.

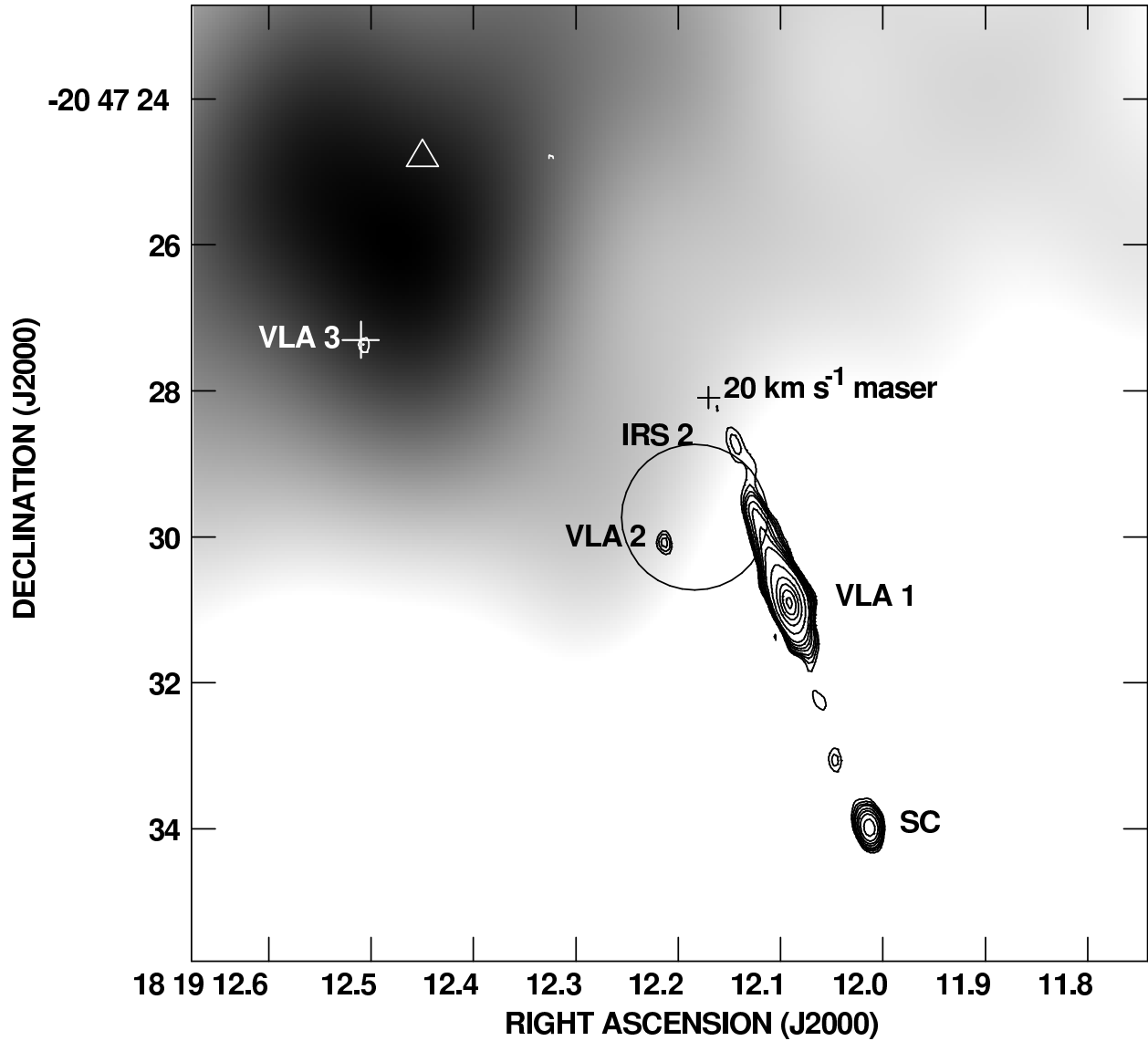


Fig. 5.— Source positions in the HH80-81 field. Contours show 3.6 cm continuum emission (Gómez et al. 1995) while greyscale shows NH_3 (1,1) emission (Gómez et al. 2003). The 20 km s^{-1} water maser is seen aligned with the thermal jet, at the border of the molecular gas. The other site of water maser emission, VLA-3, is associated with much denser molecular gas. The triangle shows the position of a 44 GHz methanol maser (Kurtz, Hofner & Vargas Álvarez, 2004) while the circle shows the approximate size and position of IRS2 (Stecklum et al. 1997).

Table 1. Observed Sources

Source	α (B1950) (h m s)	δ (B1950) ($^{\circ}$ ' ")	ΔV km s $^{-1}$	3σ (Jy)	Maser Detection
G9.88–0.75	18 07 19.3	-20 46 22	–24.3 — 144.1	0.51	N
G10.84–2.59	18 16 13.0	-20 48 49	–84.1 — 144.0	0.44	Y
G11.11–0.40	18 08 34.4	-19 31 23	–74.1 — 143.8	0.64	Y ^b
G18.15–0.28	18 22 11.6	-13 17 23	–168.5 — 168.2	0.34	N
G18.30–0.39	18 22 53.1	-13 12 08	–168.5 — 168.2	0.52	Y ^b
G19.49+0.14	18 23 16.6	-11 54 20	–168.5 — 168.2	0.34	N
G25.65+1.05	18 31 40.2	-06 02 06	–23.9 — 143.9	0.50	Y
G28.20–0.05	18 40 19.4	-04 17 06	–24.1 — 183.9	0.69	Y
G28.29–0.36	18 41 36.3	-04 21 02	–168.5 — 144.2 ^a	0.26	N
G31.28–0.06	18 45 36.5	-01 29 53	–24.1 — 193.8	0.36	Y
G31.40–0.26	18 46 57.5	-01 32 33	–24.1 — 173.8	0.38	Y
G33.13–0.09	18 49 34.3	+00 04 31	–24.1 — 143.8	0.38	Y
G35.02+0.35	18 51 29.0	+01 57 29	–24.1 — 143.8	0.35	Y
G35.57+0.07	18 53 29.9	+02 18 56	–168.5 — 168.2	0.21	N
G37.87–0.40	18 59 24.5	+04 08 27	–24.1 — 143.8	0.34	Y
G43.80–0.13	19 09 30.9	+09 30 46	–44.1 — 123.8	0.46	Y
G48.61+0.02	19 18 12.9	+13 49 43	–44.1 — 123.8	0.37	Y
G53.61+0.05	19 28 05.6	+18 13 43	–168.5 — 168.2	0.23	N
G60.88–0.13	19 44 13.7	+24 28 05	–54.1 — 113.8	0.39	Y
G69.54–0.98	20 08 09.8	+31 22 41	–54.1 — 113.8	0.42	Y
G70.29+1.60	19 59 50.1	+33 24 19	–64.1 — 53.7	0.20	Y
G76.18+0.13	20 21 53.7	+37 28 48	–168.5 — 168.2	0.26	N
G77.97–0.01	20 27 45.8	+38 51 18	–168.5 — 168.2	0.18	N
G78.44+2.66	20 17 53.0	+40 47 07	–168.5 — 168.2	0.23	N
G79.30+0.28	20 30 40.2	+40 05 49	–168.5 — 168.2	0.23	N
G79.32+1.31	20 26 22.6	+40 43 37	–168.5 — 168.2	0.21	N
G80.87+0.42	20 35 04.4	+41 25 54	–168.5 — 168.2	0.23	N
G81.68+0.54	20 37 14.2	+42 09 15	–168.5 — 168.2	0.30	Y
G106.80+5.31	22 17 40.3	+63 03 36	–134.1 — 83.8	0.38	Y
G109.85+2.10	22 54 13.5	+61 44 46	–134.1 — 73.9	0.34	Y
G110.21+2.63	22 55 03.0	+62 22 25	–168.5 — 168.2	0.21	N
G111.28–0.66	23 13 52.6	+59 45 38	–228.5 — 108.2	0.26	N
G111.61+0.37	23 13 21.3	+60 50 51	–128.5 — 108.2	0.23	N

^aNo data between -35.9 and -24.3 km s $^{-1}$.

^bNew detection, not previously reported in the literature.

Table 2. Observed Maser Parameters

Source	S_{\max} (Jy)	V_{\max} km s^{-1}	ΔV km s^{-1}	$\int S \, dV$ (Jy km s^{-1})
G10.84–2.59	205.1	–72.3	–80.6 - 4.2	954.2
G11.11–0.40	2.7	+11.8	5.2 ^a	3.7
G18.30–0.39	0.8	+28.4	1.6 ^a	0.7
G25.65+1.05	452.3	+41.3	–15.2 - 48.0	1142.4
G28.20–0.05	2.3	+94.1	85.4 - 99.4	6.5
G31.28–0.06	29.8	+108.5	80.5 - 119.9	53.1
G31.40–0.26	8.4	+91.8	48.1 - 97.5	24.1
G33.13–0.09	36.6	+66.1	64.0 - 88.0	138.2
G35.02+0.35	4.1	+44.1	43.0 - 57.6	9.4
G37.87–0.40	11.4	+58.8	4.8 ^a	22.5
G43.80–0.13	1022.1	+42.1	19.0 - 93.0	1574.1
G48.61+0.02	61.2	+2.3	–12.5 - 44.5	272.2
G60.88–0.13	20.6	+23.3	18.1 - 32.9	24.4
G69.54–0.98	579.8	+15.1	–52.9 - 63.1	622.7
G70.29+1.60	4.8	–33.8	–45.9 - –14.5	23.1
G81.68+0.54	4.7	–8.2	–10.7 - 0.7	9.8
G106.80+5.31	14.5	–3.1	–16.3 - 3.3	17.5
G109.85+2.10	107.4	–9.0	–19.2 - 20.4	162.5

^aSingle feature full width zero intensity.